Direct Numerical Simulations of coolant injection through a porous layer for transpiration cooling in hypersonic flow

Adriano Cerminara*, Ralf Deiterding†, Neil D. Sandham ‡
Aerodynamics and Flight Mechanics Research Group
University of Southampton, Southampton, Hampshire, SO17 1BJ, United Kingdom

August 27, 2019

Abstract

The present work describes latest advancements in the context of high-fidelity numerical simulations of flow through porous media in a hypersonic freestream. The aim of this work is to find an appropriate solution to the challenging requirement of accurately resolving complex multiscale flow features combined with minimum computational cost, as well as to design a methodology that allows predictive capabilities for the aerothermal design of new-generation thermal protection systems (TPS) for hypersonic vehicles. The requirement of an accurate and reliable solution which captures the main physical insights of the flow is particularly strict when dealing with hypervelocity flows, because of the dramatic consequences that aerodynamic heating and transition to turbulence have on the vehicle structure integrity in this flow regime. A numerical study is presented which investigates, through direct numerical simulation (DNS) of the Navier-Stokes equations, the main characteristics of a hypersonic flow at Mach 5 over a flat plate with coolant injection provided from a layer of distributed porosity that mimics the properties of a real porous material sample used in a ground-test experiment. The numerical simulations are performed using a 6^{th}-order hybrid WENO-central scheme, with a structured adaptive mesh refinement (SAMR) technique that provides adequate grid resolution in the very small scales of the porous region. A regular arrangement of staggered cylinders is considered to model the porous structure, and the correlation between pressure drop and flow rate across the porous layer is simulated for different cylinder diameters and at the same experimental flow conditions. In particular, based on a former computational study available in the literature, a multiscale numerical methodology is developed and assessed for inner particle diameters from 12 μm up to 96 μm, which allows an equivalent Darcy-Forchheimer behaviour relative to a real small-scale porous sample to be replicated by a porous layer with significantly higher pore scales.

*Research Fellow
†Associate Professor of Aerospace Engineering
‡Professor of Aerospace Engineering

1 Introduction

In hypersonic flows, where aerodynamic heating compromises the vehicle structure integrity, the film cooling technique [1, 2] represents a valid solution to suppress the heat loads experienced by the surface material. This technique is aimed at injecting coolant in the hot boundary layer to form a thin film of cold fluid adjacent to the wall, thus reducing the wall heat flux. We can distinguish two different injection strategies, namely effusion cooling [3, 4], and transpiration cooling [5, 6]. The former provides injection through localised holes, and is typically used for thermal protection of turbine blades surfaces, in which cooling occurs through a turbulent mixing layer. The latter, in contrast, takes advantage of the transpiration capabilities of a porous material to provide a more uniformly distributed coolant film. Due to the enhanced heat exchange occurring between the coolant and the structure through the multiple pores of micrometer dimension [6], the transpiration cooling systems represent an efficient solution to the aerodynamic heating.

In a supersonic-hypersonic flow, however, the wall cooling requirement combines with the requirement of increasing the laminar run of the boundary layer, i.e. delaying transition. For this reason, injection through two-dimensional slots is in general preferred, as it reduces the 3D effects associated with hole injection [7, 8, 9]. This suggests that for transpiration cooling systems the homogeneity of the injected flow over the surface as well as the injection velocity, or the blowing ratio, assume a very important role for the stability characteristics of the boundary layer, and the associated cooling performance.

Accurate analysis and prediction of the cooling performance as well as the effects on the boundary-layer stability are needed to enable the correct design and optimisation of an efficient transpiration cooling system for hypersonic vehicles. This requires the details of the flow features at the pore scale to be accurately captured by a numerical study, without the need of simplified theoretical or empirical models that account only for a certain number of parameters and are generally dependent on certain specified conditions. For example, among the several models available in the literature describing the Darcy-Forchheimer drag opposed by a porous material to the traversing flow in the presence of a pressure drop, Ergun's empirical model [10] is known to provide good results for certain geometrical microstructures of the porous layer, i.e. for granular media as in the case of packed beds of spheres, and dependent on the range of porosities. The coefficients defined in the model change, in general, when different geometries are considered. Another factor influencing the accuracy of the model is the roughness of the solid particles, as shown by Macdonald et al. [11], in their revision of Ergun's equation. Several correlations between pressure drop and flow rate have been developed by different authors, which mostly differ in the coefficients provided to weight the two contributes of the friction drag and the pressure drag, namely the Darcy and the Forchheimer drag, respectively. A comprehensive list of the correlation models is provided by Erdim et al.[12], who specify also a Reynolds number range of application of Ergun's model [10].

The difficulty in deriving a universal model of the pressure drop - flow rate correlation stands mainly in the description of the permeability (K) of the interior material

structure. The well-known permeability model developed by Kozeny [13] correlates the permeability to the porosity (ϵ) and to the specific surface area per unit volume of the pores (S) through a dimensionless constant (c_0) called Kozeny constant. If the porosity is known for a given porous sample, an accurate estimation of the pore surface area is in general very difficult, especially for complex pore geometries, as in the case of the rocks and the porous materials studied in geological sciences. Moreover, although a value of 1/5 is generally considered for the Kozeny constant, it is obviously not universal, and will change for pores with different geometrical characteristics. A numerical study of the Kozeny constant for random packings of spheres as well as for a soil sample can be found in [14], in which it is shown that the Kozeny constant varies with the sphere radius.

The Kozeny model was then modified by Carman [15], who provided a more general form of the model introducing the dependence on the average path length of the streamlines through the porous layer, i.e. the tortuosity. However, again, it is not simple to measure the tortuosity of a material and there exists no universal law that gives the correct tortuosity given a material with certain properties. A numerical study aimed at evaluating the dependence of the tortuosity from the porosity was given by Matyka et al. [16], in which the authors fitted their numerically obtained data at different porosities to four different tortuosity-porosity models provided by other authors, each one dependent on a adjustable parameter.

Hence, due to the several parameters influencing the accuracy of a model in porous geometries of different complexity, the capability of predicting the Darcy-Forchheimer behaviour by directly simulating the flow through the porous structure plays an important role, especially in the presence of the complex hypersonic flow physics interacting with the surface of the porous material. However, the main challenges of the simulation approach can be summarised as i) the difficulty of reproducing in the computational mesh the exact internal geometry, and ii) the computational cost associated to the small micrometer scales of the interior pores, in particular in the case of direct numerical simulations. In the case of a relatively simple internal porous structure, e.g. random packagings of spheres, different computational studies [17, 18, 19] have shown that an arrangement of staggered cylinders with constant radius in two-dimensional (2D) simulations provides in general good results in agreement with the empirical model of Ergun's model over a wide range of porosities. In the work of Lee and Yang [18], in particular, the authors adopt a numerical model of a single pore cell in virtue of the periodicity of the flow inside a regular bank of staggered cylinders, and obtain results in a very good agreement with Ergun's model for a wide range of granular Reynolds numbers and for different porosities.

The objective of our study is to present and assess a methodology, based on Lee and Yang's approach [18], which allows multiscale simulations of the flow through porous media in a hypersonic freestream. The aim of this multiscale methodology is to mimic the Darcy-Forchheimer behaviour of a real experimental porous material, characterised by very small pore length scales, by means of a porous layer with significantly higher pore scales that develop an equivalent Darcy-Forchheimer drag. Such an approach would make direct numerical simulations of the flow through porous media affordable, thus allowing the complex flow features of injection in a hypersonic boundary layer to be accurately resolved without the need of simplified models. A validation is first

performed against the results of Lee and Yang [18] for a case with no crossflow on the surface of the porous layer, then a relation for the pressure drop in function of a characteristic Reynolds number is derived, which enables rescaling of the pore size for an equivalent Darcy-Forchheimer bahaviour. The multiscale methodology is assessed with application to a real reference experimental case.

2 Numerical method

2.1 Governing equations

We consider numerical solutions of the three-dimensional Navier-Stokes equations for compressible flows, written in conservation form, under the assumption of a perfect gas. The set of non-dimensional conservation equations in Cartesian coordinates can be written as

$$\frac{\partial \rho}{\partial t} + \frac{\partial \rho u_j}{\partial x_j} = 0 \,, \tag{1}$$

$$\frac{\partial \rho u_i}{\partial t} + \frac{\partial \rho u_i u_j}{\partial x_j} = -\frac{\partial p}{\partial x_i} + \frac{1}{\mathrm{Re}} \frac{\partial \tau_{ij}}{\partial x_j} \,, \tag{2}$$

$$\begin{aligned} \frac{\partial \rho E}{\partial t} + \frac{\partial \left(\rho E + \frac{p}{\rho}\right) u_j}{\partial x_j} = & -\frac{1}{(\gamma-1)\mathrm{RePr}M^2} \frac{\partial}{\partial x_j}\left(\frac{\partial \kappa T}{\partial x_j}\right) \\ & + \frac{1}{\gamma \mathrm{Re} ScM^2} \frac{\partial}{\partial x_j}\left(\rho D \sum_k \frac{\partial c_k}{\partial x_j} c_{p,k} T\right) + \frac{1}{\mathrm{Re}} \frac{\partial \tau_{ij} u_i}{\partial x_j} \,, \end{aligned} \tag{3}$$

$$\frac{\partial \rho c_k}{\partial t} + \frac{\partial}{\partial x_j}\left(\rho c_k u_j - \rho D \frac{\partial c_k}{\partial x_j}\right) = 0 \,. \tag{4}$$

The terms ρ, ρu, ρv, ρw and ρE are the conservative variables of the system of equations, where ρ is the density, u, v and w are the velocity components respectively in the x-, y- and z-direction, and E is the total energy per unit mass. In the flux vectors, the terms p, T, τ_{ij}, and μ are respectively the pressure, the temperature, the components of the viscous stress tensor, and the dynamic viscosity of the flow. The non-dimensional quantities are obtained through normalisation of the dimensional variables with their freestream reference values: the velocity components are normalised with the freestream main velocity (U^*_∞), the density is normalised with the freestream density (ρ^*_∞), the viscosity is normalised with the freestream dynamic viscosity (μ^*_∞), the temperature is normalised with the freestream temperature (T^*_∞), the total energy is normalised with the square of the freestream mean velocity (U^{*2}_∞), while the pressure and viscous stresses are normalised with the term $\rho^*_\infty U^{*2}_\infty$, related to the freestream dynamic pressure. Note that the superscript $(^*)$ is used to denote

dimensional values. The characteristic length chosen to normalise the length scales is the boundary-layer displacement thickness (δ^*). The time scales are normalised with respect to the fluid dynamic characteristic time (δ^*/U^*_∞), based on the velocity of the undisturbed flow and on the characteristic length. The terms Re, Pr, M, and γ are respectively the Reynolds, Prandtl and Mach numbers, and the ratio of specific heats ($\gamma = c^*_p/c^*_v$), i.e. the dimensionless parameters of the flow. The Reynolds number is defined with respect to the boundary-layer displacement thickness of the similarity solution, as $\mathrm{Re} = (\rho^*_\infty U^*_\infty \delta^*)/\mu^*_\infty$; the Prandtl number is set to 0.72 for air, and γ is equal to 1.4, as we are considering a perfect gas model. The dynamic viscosity of the mixture is expressed by means of Wilke's rule as,

$$\mu = \sum_k \frac{X_k \mu_k}{\sum_l X_l \phi_{kl}} \,, \tag{5}$$

and the mixture thermal conductivity as,

$$\kappa = \sum_k \frac{X_k \frac{\mu_k c_{p,k}}{\mathrm{Pr}_k}}{\sum_l X_l \phi_{kl}} \,, \tag{6}$$

in which the viscosity of each species is computed through the power law as $\mu^*_k = \mu^*_{k,\infty} (T^*/T^*_\infty)$. In relations 5 and 6, the term X_k represents the species mole fraction, which can be expressed as,

$$X_k = \frac{\frac{c_k}{M_k}}{\frac{c_1}{M_1} + \frac{c_2}{M_2}} \,, \tag{7}$$

where M_k is the molecular weight of the k-species. Note that we are considering a mixture composed by only two species, i.e. a binary mixture, for which $k = 1, 2$, and $l = 1, 2$. The term ϕ_{kl} is a function of each species viscosity and molecular weight, which is defined as,

$$\phi_{kl} = \frac{1}{\sqrt{8}} \left(1 + \frac{M_k}{M_l}\right)^{-1/2} \left[1 + \left(\frac{\mu_k}{\mu_l}\right)^{\frac{1}{2}} \left(\frac{M_l}{M_k}\right)^{\frac{1}{4}}\right]^2 \,. \tag{8}$$

To complete the definition of the transport properties of the mixture we need to define the mixture diffusivity, D, which is expressed as a function of the local temperature and pressure through the relation [20],

$$\mathrm{D} = \mathrm{D}_{1,2} = 0.0018583 \frac{\sqrt{T^3 \sum_k M_k^{-1}}}{p d^2 \Omega_d} \,, \tag{9}$$

where the d represents the characteristic molecular diameter, which for the mixture can be taken as an average between the molecular diameters of the single species, i.e. $d = 1/2\,(d_1 + d_2)$; whereas the term Ω_d represents the transport collision integral of the binary mixture. This is a function of the reduced temperature $T_{red} = k_B T^*/\epsilon$, where $k_B = 1.3806488 \times 10^{-23}$ J/K is the Boltzmann constant and ϵ is the mixture attractive energy between two molecules in a binary mixture, defined as $\epsilon = \sqrt{\epsilon_1 \epsilon_2}$.

The relation used for the evaluation of the collision integral for the Lennard-Jones (12-6) potential is [21]

$$\Omega_d = \Omega_{1,2} = \left(A/T_{red}^B\right) + [C/\exp(DT_{red})] + [E/\exp(FT_{red})] + [G/\exp(HT_{red})] \tag{10}$$

with coefficients A, B, C, D, E, F, G, H given in [21]. The viscous stresses are defined in terms of the velocity derivatives, under the assumption of a Newtonian fluid, as

$$\tau_{ij} = \mu \left[\frac{\partial u_i}{\partial x_j} + \frac{\partial u_j}{\partial x_i} - \frac{2}{3}\delta_{ij} \frac{\partial u_k}{\partial x_k} \right] . \tag{11}$$

Finally, the system of the governing equations is closed by the relation for the total energy,

$$E = c_v T + \frac{1}{2}\left(u^2 + v^2 + w^2\right) , \tag{12}$$

and by the equation of state,

$$p = \frac{1}{\gamma \mathrm{M}^2} \rho R T . \tag{13}$$

The specific heats at constant volume and pressure, namely c_v and c_p respectively, as well as the gas constant R, represent mixture properties, which are given as [8]

$$c_v^* = c_1 c_{v,1}^* + c_2 c_{v,2}^* , \tag{14}$$

$$c_p^* = c_1 c_{p,1}^* + c_2 c_{p,2}^* , \tag{15}$$

and

$$R = c_p - c_v . \tag{16}$$

2.2 Numerical scheme

The finite-volume method used to solve numerically the governing equations consists of a 6^{th}-order central differencing (CD) scheme in space for both inviscid and viscous fluxes, combined with a 6^{th}-order weighted-essentially-non-oscillatory (WENO) scheme for shock capturing, along with a 3^{th}-order Runge-Kutta method for time integration. The so-called WENO-CD scheme is provided with a switch function that turns on/off the shock-capturing scheme at discontinuities and in smooth flow regions, respectively, and has been validated over the past years for several types of compressible high speed flow configurations [22, 23, 24, 25, 26, 27].

A very important feature of our code that enables high-resolution in the very small length scales of the slot/porous injector, allowing for multiscale simulations, is represented by the structured adaptive mesh refinement (SAMR) method. This technique, decribed in [28] allows consecutive higher grid refinement levels to be dynamically added in the high-gradient flow regions in a patch-wise fashion, thus providing higher

numerical stability and solution accuracy in the flowfield as well as minimising the computational cost.

2.3 SAMR approach

The key feature of our numerical method to accurately resolve all the flow regions in a multiscale system is the SAMR strategy [28, 29]. With this approach, consecutive higher grid refinement levels are dynamically added into the high-gradient flow regions in a patch-wise fashion, thus providing higher numerical stability and solution accuracy in the flowfield as well as minimising the computational cost. In the patch-wise refinement strategy, the cells pertaining to high-gradient zones of some prescribed physical quantities (e.g. density and velocity components) are flaggered by error indicators (e.g. gradient higher than a certain imposed threshold) and clustered into rectangular boxes, which define the regions of the computational domain requiring refinement. Subgrid patches with a prescribed refinement factor and aligned to the coarse grid are successively added onto the coarser level to form a hierarchy of embedded refined grid patches.

As described in [28], the sequence $l = 0, ..., l_{max}$ of successively higher refinement levels of the grid hierarchy is discretised with a refined mesh width $\Delta x_{n,l}$, and a refined time step Δt_l, with $n = 1, ..., d$ defining the discretisation direction and d the maximum dimension. Denoting with $r_l \geq 2$ the (integer) refinement factor at each level, the mesh spacings of the levels $l > 0$ are r_l-times smaller than the corresponding sizes at level $l - 1$ ($r_0 = 1$ denotes the coarsest, or base, grid level). Hence, the grid spacings in each direction and the time step at the level l are linked to the corresponding values at the coarser level $l - 1$ through the relations

$$\Delta x_{n,l} = \frac{\Delta x_{n,l-1}}{r_l} \ , \ \Delta t_l = \frac{\Delta t_{l-1}}{r_l}. \tag{17}$$

This means that the time-step-to-cell-size ratios in each direction remains constant between all the grid levels, i.e.

$$\frac{\Delta t_l}{\Delta x_{n,l}} = \frac{\Delta t_{l-1}}{\Delta x_{n,l-1}} = ... = \frac{\Delta t_0}{\Delta x_{n,0}} \ , \ n = 1, ..., d. \tag{18}$$

Hence, the Courant-Friedrichs-Lewy (CFL) condition is basically not affected, which preserves numerical stability at all the grid levels.

The AMROC framework [28] implements the SAMR method discretisation independent in one to three space dimensions and is fully parallelized for distributed memory systems. With its parallel distribution strategy, described in detail in [28], the overlapping ghost-cell regions of neighboring patch blocks are synchronized over processor borders as boundary conditions are applied. The communication between processors is achieved through the MPI-library and a space filling curve algorithm is used for load-balanced data distribution.

3 Flow conditions and settings

The freestream conditions correspond to $M = 5$, $\mathrm{Re} = 12600$, $T^*_\infty = 76.6$ K, and the wall temperature is fixed to the room temperature, $T^*_w = 290$ K. These conditions replicate the freestream conditions of the experimental tests made by [30]. The flow is initialised with the laminar boundary layer from the similarity solution. Different 2D preliminary simulations have been performed for different domain sizes. As an initial test case, we consider a small flat-plate domain with periodic boundary conditions in the streamwise direction, outflow condition at the top boundary, no-slip adiabatic condition at the plate wall ($y = 0$) and plenum condition at the bottom boundary ($y = -2$). The plenum boundary condition consists of imposing the stagnation pressure (p_0) and stagnation temperature (T_0) at the bottom boundary, to simulate the presence of an underneath plenum chamber that drives vertical fluid motion in the porous layer. The computational domain and the corresponding mesh are shown in figure 1, with the initial streamwise velocity field plotted in figure 1a. The base grid size is $N_x \times N_y = 50 \times 126$, and the domain sizes in the streamwise and vertical directions are $L_x = 5$ and $L_y = 10.5$, respectively, including the porous layer thickness. These grid and domain size settings provide cell sizes in the coarse (base) grid level of $\Delta x = 0.1$ and $\Delta y = 0.083$.

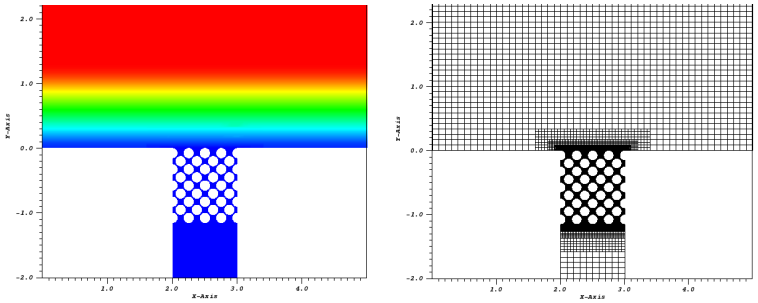

(a) u field at time $t = 0$ (b) mesh with 5 AMR levels

Figure 1: Computational domain, streamwise velocity u plotted (a), and corresponding mesh (b)

For the present test case, the plenum pressure and temperature were set to $p_0 = 1.5p_\infty$, and $T_0 = T_w$. Thus, a pressure ratio of 1.5 is imposed between the plenum chamber and the wall to generate the injection flow. To increase numerical stability in the initial time steps, the plenum pressure was linearly increased with time from an initial uniform value of p_∞ to the target value of $p_0 = 1.5p_\infty$. Note that the condition $p_0 = p_\infty$ corresponds to a condition without injection, due to the difference between the pressure in the plenum chamber and the pressure at the wall being zero.

In figure 1b the different AMR levels and their localised position within the domain can be seen. Five overall levels are present, with the finer being concentrated in the region of the pores. Each finer level is embedded in the next coarser one. This arrangement of the AMR levels allow the flow features within the porous layer to be

captured with optimised computational cost. The porous layer has a nondimensional thickness of 1.2 and a length of 1. It consists of a regular arrangement of equally-spaced circular elements (2D cylinders) with a radius of $r = 0.078$ in this example (corresponding to 78 μm), representing the solid particles. In particular, a staggered arrangement is considered between different rows of cylinders, with a 45° inclination angle for a straight line connecting two adjacent staggered cylinder centres at two different y-locations. The distances between two adjacent particles both along the x- and y-directions (same distance), as well as along a 45° diagonal, follow from the choice of the radius (r) and the porosity (ϵ). Hence, r and ϵ represent the main parameters of the porous layer. In this case we set a porosity of 42 %, which is representative of the real experimental porous samples.

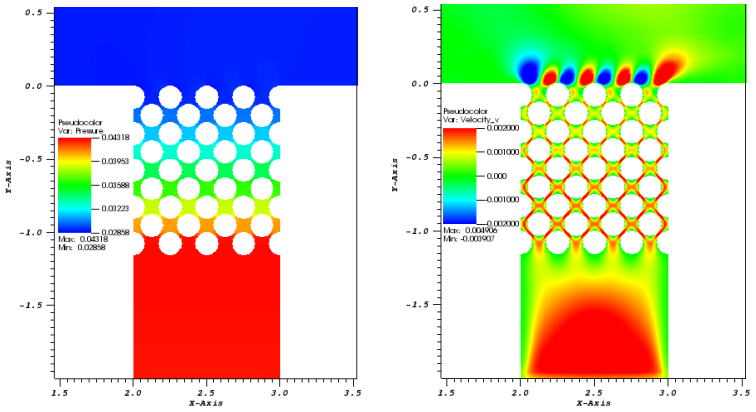

(a) pressure field (b) vertical velocity (v) field

Figure 2: Instantaneous pressure field (a), and vertical velocity field (b)

By defining the distance between two adjacent cylinder centres along a 45° diagonal as l_d, the minimum length scale within the porous layer is $d_{min} = l_d - 2r$, which represents the distance between the two solid surfaces of the staggered adjacent cylinders. The strict positive value of this minimum distance represents a constraint for the cylinder arrangement, which does not allow to consider small porosity levels. In fact, below a certain porosity level, d_{min} becomes negative, meaning that the solid particles along the diagonal would penetrate each other, thus not allowing the fluid to flow through.

In figure 2 instantaneous results for the pressure field and the vertical velocity field in the porous layer are shown. After a certain time, the pressure in all the volume underneath the porous layer (representing the plenum chamber) reaches a uniform constant value equal to p_0. A linear pressure gradient from p_0 (at the lower surface) to p_∞ (at the upper surface) is formed across the porous layer in the y-direction, which drives the injected flow through according to the Darcy-Forchheimer relation,

$$\frac{\Delta p}{\delta} = \frac{\mu}{K} U + C\rho U^2 \,, \tag{19}$$

in which δ is the thickness of the porous layer, K is the material permeability, U is the superficial velocity averaged through the porous layer, and C is a constant known as Forchheimer constant. The first term at the right hand side of equation 19, i.e. the Darcy term, represents the drag contribution related to the viscous effects and to the material permeability. The second term, i.e. the Forchheimer term, represents the contribution relative to the inertial effects, and is relevant for high values of the velocity and of the solid particles size, hence high values of the local Reynolds number, as we will see in detail later in this work.

Figure 2b shows details of the vertical velocity within the porous layer. This is an instantaneous solution, in which the lower part of the porous layer is characterised by higher values of the velocity, thus indicating that the flow is gradually ascending across the thickness of the porous layer. Moreover, as can be seen, the local peak of the vertical velocity within the pores is reached at the restriction location, i.e. at the point of minimum distance (d_{min}) between two adjacent solid particles.

Figure 3 shows the face-centred cubic structure used in our computational approach to model the porous miscrostructure of the material. By defining a side length of the square area as l, the porosity ϵ, i.e. the ratio between the void space inside the square and the total area, can be expressed as

$$\epsilon = \frac{l^2 - 2\pi r^2}{l^2} \, . \tag{20}$$

Once having assigned a value for the porosity and a value for the cylinder particle radius, the size of the square structure can be found as

$$l = r\sqrt{\frac{2\pi}{1-\epsilon}} \, , \tag{21}$$

and the minimum distance in our porosity structure can be expressed as

$$d_{min} = l\frac{\sqrt{2}}{2} - 2r \, . \tag{22}$$

In the considered test case, with reference to figures 1 and 2, the minimum distance is $d_{min} = 0.025$, corresponding to 25 μm.

The solid particles are simulated through an embedded boundary method, i.e. the ghost fluid method, in which cells inside the solid surface are taken out from the CFD domain of the interior fluid, and trated as ghost cells. A more detailed description of the ghost fluid methodology can be found in [31].

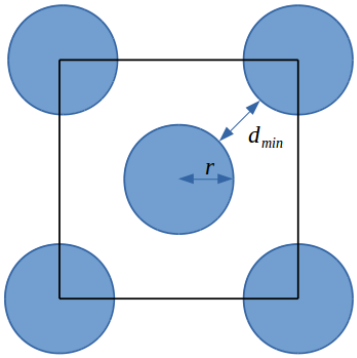

Figure 3: Sketch of a pore cell structure

Figure 4 shows an example of the AMR strategy applied to a generic staggered cylinder porous structure. Solution accuracy has been obtained through the use of five refinement levels, for a total of six grid levels. In this example test case, a high porosity ($74\,\%$) has been considered, with the radius of each particle being $0.05\,\mathrm{mm}$ and the minimum distance between two neighbour elements equal to $0.076\,\mathrm{mm}$. As can be observed, in this example the finest grid level is used around each solid particle, which captures the boundary layer formed at the cylinder surface and provides a smoother surface in the Cartesian mesh.

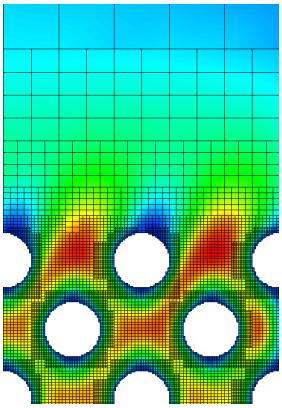

Figure 4: AMR levels distribution. Vertical velocity field plotted

With reference to the initial test case described in Section 3, with results shown in figures 1 and 2, a grid refinement study with different AMR levels has been carried out in order to evaluate the grid requirements for a case of equivalent porosity.

Figure 5 shows the solution sensitivity of the blowing ratio (i.e. $F = \rho v|_{inj}$) at the porous layer surface ($y = 0$) to different AMR levels, namely four, five and six levels. Results show that a good agreement between the different grid levels is obtained for the blowing ratio. The grid with six levels, however, shows better details at the curve

inflection points located at $\rho v = 0$ in the shear layer of the vertical velocity, formed just downstream of each injection jet.

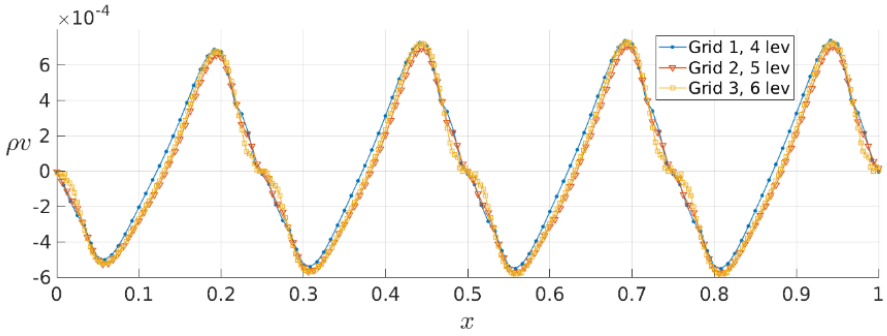

Figure 5: Grid study, on a small porous layer sample, for different AMR levels based on the blowing ratio at the surface of the porous layer ($y = 0$)

4 Results

4.1 Preliminary results

After having peformed the initial test of the boundary conditions and the grid resolution requirements on the small flat-plate domain, representative of a small sample of the porous layer, we now perform 2D simulations on a long flat-plate domain, which is representative of the real experiment carried out at Oxford University on the UHTC porous sample. The material sample used in the experiments [30] was $5\,\mathrm{mm}$ thick - $39\,\mathrm{mm}$ long, with a porosity of 42 %, as mentioned above. A generic picture of the computational domain can be seen in figure 6, where the mean pressure field is shown, obtained from a plenum pressure of $p_0 = 1.9 p_\infty$. The domain size is $L_x = 150$ in the streamwise direction and $L_y = 24.5$ in the vertical direction. The front edge of the porous layer is located at the position $x = 38$ in our computational domain, which corresponds to a distance of 160 mm from the plate leading edge in the experiment.

The characteristic length is the boundary layer displacement thickness at the inflow from the similarity solution, i.e. $\delta_0^* = 1$ mm. The porous layer thickness is 5 mm as in the experiment, and the plenum chamber is represented by an underneath region of 1 mm thickness. In this case, due to the higher size of the computational domain and of the porous layer compared to the previous small domain, cylinders with a larger radius have been considered, i.e. $r = 200\,\mu$m, which provides a minimum interior length scale of $d_{min} = 0.0619$ (corresponding to about $62\,\mu$m). Hence, considering that in the small-domain simulations described in Section 3 the minimum length scale was $25\,\mu$m, the grid requirements relative to the present long-domain case are about half of the small-domain case. In fact, the base grid size is $N_x \times N_y = 1500 \times 294$, and the corresponding spacings are the same as those used in the small-domain case, i.e. $\Delta x = 0.1$ and $\Delta y = 0.083$. However, due to the higher minimum distance, only 3 overall levels are considered in the AMR framework in this case, which provide a

resolved solution within the porous layer. An extrapolation boundary condition has been used at the inflow of the domain, and an outflow condition at the outlet boundary.

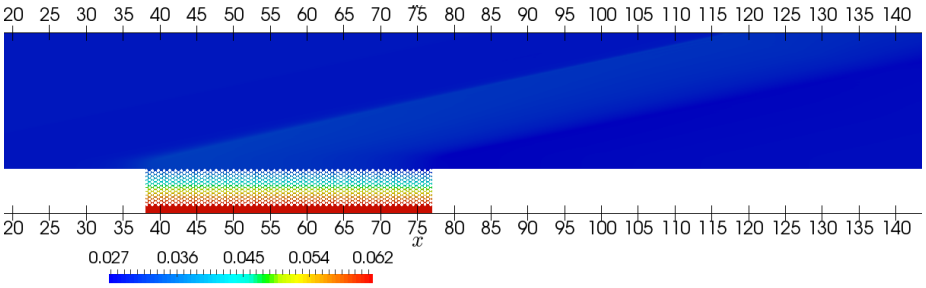

Figure 6: Pressure field for the case of injection through a porous layer made of cylinders with radius of 200 μm

Figures 7, 8 show qualitative results for the density and the Schlieren image for the considered case. The results show the physical details of the boundary layer thickening due to the flow injection, and of a weak shock generated just upstream of the porous layer. The plenum pressure relative to these results is $p_0 = 1.9p_\infty$.

Different simulations have been performed at different plenum pressures, to observe the effect on the blowing ratio ($\rho v|_{inj}$) distribution along the surface, with results plotted in Figure 9. As can be seen, the injection profile assumes a flat shape in the middle of the porous surface, while showing an increasing trend along x at the boarders with the solid wall. In particular, an evident increase is observed near the right edge. This is in general caused by the effect of the porous injection on the local pressure within the boundary layer. In particular, the pronounced increase of the injection rate observed in the downstream region of the porous surface is generated by the expansion of the hypersonic flow outside the boundary layer downstream of the shock generated at the beginning of the porous layer. To understand this effect we should refer to figures 7, 8. Downstream of the shock, the boundary layer is observed to increase approximately linearly with the streamwise distance, however, near the exit of the porous layer, it assumes a convex shape as its thickness converges to the value assumed at the solid wall downstream of the porous layer. The convex shape of the boundary-layer thickness produces the expansion of the external hypersonic flow, and, as the pressure within the boundary layer can be in general considered constant along the y-direction, also the fluid at the wall will experience the same expansion. An expansion at the porous layer surface translates in a higher pressure drop across the porous layer, between the plenum pressure and the exit pressure, which results in a higher blowing ratio.

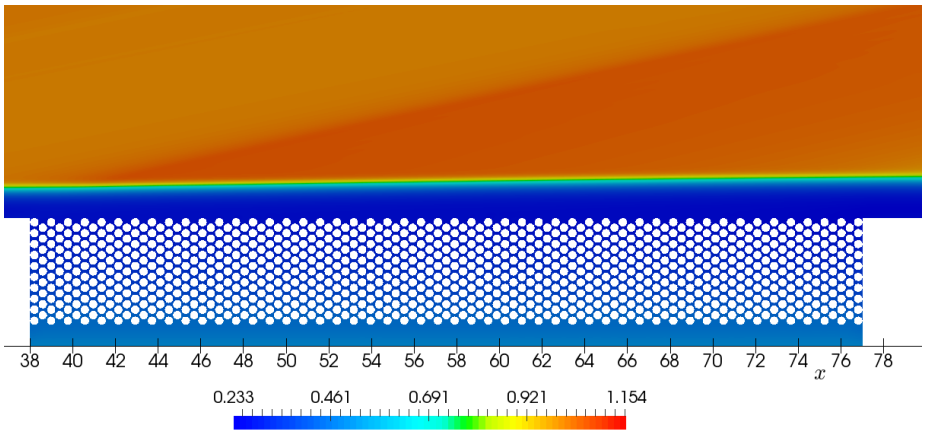

Figure 7: Density field for the case of injection through a porous layer made of cylinders with radius of 200 μm

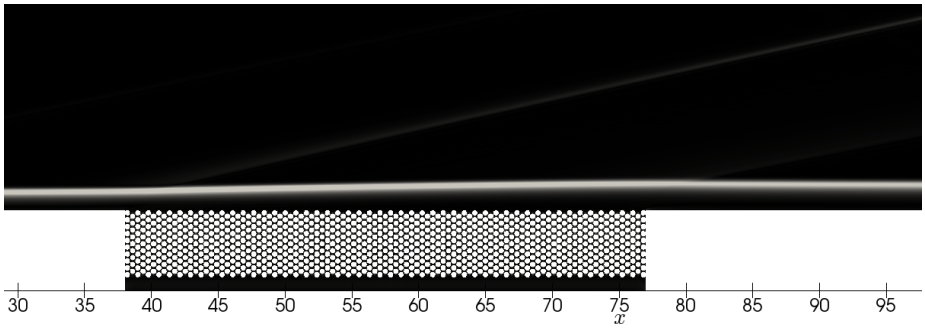

Figure 8: Schlieren for the case of injection through a porous layer made of cylinders with radius of 200 μm

The preliminary simulations allowed a grid study to be used as a reference for the resolution requirement in cases with different size of the computational domain, as well as to make some initial observations about the physical features related to the blowing ratio along the sample surface and its dependence from the plenum pressure. The calibration and validation of our porous computational model with the real experimental injection conditions will be the subject of the next section.

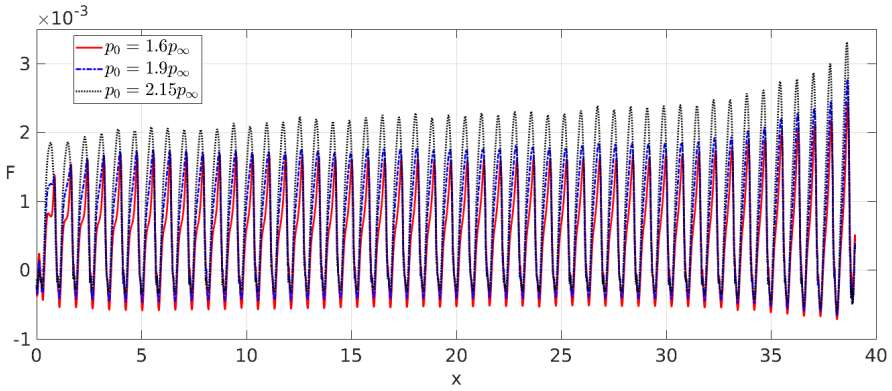

Figure 9: Blowing ratio at different plenum pressures

4.2 Multiscale approach

In order to correctly replicate the experimental conditions, we need to simulate the experimental blowing ratio resulting from the porous injection, which, in turn, is correlated to the plenum pressure and to the permeability characteristics of the sample material used in the experiment. In other words, we need to replicate the Darcy-Forchheimer behaviour (i.e. the drag opposed by the porous layer to the injection at a certain plenum pressure) of the material in the real experimental case. With reference to equation 19, the Darcy-Forchheimer behaviour of the porous layer depends on two parameters, namely the material permeability, K, and the Forchheimer constant, C. In our case, due to the very small interior length scales of the real porous material (pore size of about $1\,\mu$m $-4\,\mu$m)[30], the Forchheimer effects can be considered negligible [18], and the Darcy-Forchheimer model simplifies significantly, reducing effectively to the Darcy term.

The material permeability depends in general on the porosity and on the geometrical patterns of the interior pores. A well-known and widely used model of permeability was developed by Kozeny [13], and is expressed as

$$K = c_0 \frac{\epsilon^3}{S^2} \,, \tag{23}$$

with the coefficient c_0 typically assuming a value of 1/5. The term S represents the superficial area of the pores per unit volume. It should be mentioned that equation 23 has been expressed in the form provided by [16], as different authors express the permeability relations in a different way, dependent on considering the solid mass fraction instead of the porosity, or the coefficient at the denominator rather than at the numerator (e.g. in [14]). Equation 23 was then modified by Carman [15] to include the effects of the tortuosity T, i.e. the average path length of the flow streamlines within the porous medium. In this modified form, equation 23 can be re-written as [16]

$$K = c_0 \frac{\epsilon^3}{T^2 S^2} \,. \tag{24}$$

Although the Kozeny-Carman model, equation 24, does not represent a universal law for the permeability of a porous material, it was shown to provide good results for both random and periodic packagings of spheres, as in the case of granular media [14, 10], and for a large range of porosities.

Now, one (obvious) option for the correct simulation of the real Darcy-Forchheimer behaviour consists in imposing the same plenum pressure and the same permeability as the real experimental case to our porous structure. However, as the permeability depends on the pore size through the term S, this would require us to design a porous structure with the same interior length scales as in the real material sample (i.e. $1\,\mu$m $-4\,\mu$m). However, such small length scales would make numerical simulations unaffordable. Our objective is, instead, to design a porous structure that mimics the real material Darcy-Forchheimer behaviour, but at considerably higher interior length scales, such to allow direct numerical simulations of the full domain.

In order to cope with the small (micrometer level) length scales within the porous layer in comparison with the much larger length scales of the porous layer sample and the plate size, a multiscale approach has been developed and tested, which is based on the computational work of Lee and Yang [18], and is described as follows: i) first, the computational approach of Lee and Yang [18] is described in details in Section 4.2.1; then ii) we present a validation study of our computational results with respect to Lee and Yang's [18] model in Section 4.2.2; and iii) finally in Section 4.2.3 we present an extension of the model that allow equivalent solutions at different pore scales to be achieved (multiscale approach), and we validate our proposed methodology with reference to the experimental case [30].

4.2.1 Lee and Yang's computational model

Let us consider a 2D porous layer with periodic cell elements modelled as a regular distribution of equal-radius cylinders in a staggered position, as the face-centred structure sketched in figure 3. As suggested by Lee and Yang[18], due to the geometrical periodicity, the dimensionless steady state solution of the flowfield between two adjacent particles along the diagonal (normalised with the pressure drop between the cylinders) in the face-centred structure is the same for the other quarters. Hence, the reference periodic fluid-dynamic domain reduces to a single quarter of the face-centred structure, as shown in figure 10, which can be defined as a pore cell.

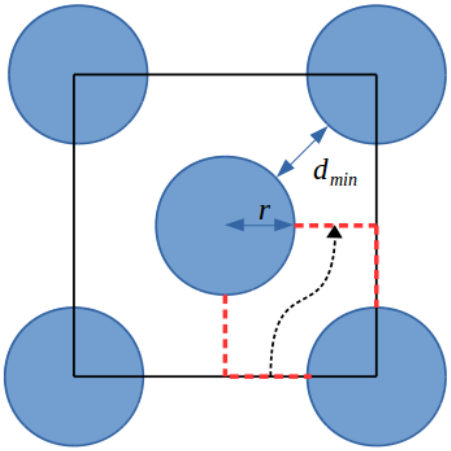

Figure 10: Periodic fluid-dynamic domain boundaries (red dashed lines) identifying a single pore cell. The dashed line arrow represents the fluid path

A detailed sketch of a single pore cell in the periodic flow through a bed of staggered cylinders is represented in figure 11, where L is the distance between the two staggered cylinder centres, and D is the cylinder diameter. Such a configuration, along with the 3D corresponding configuration of staggered spheres in a 3D domain, has been demonstrated [18, 17, 19] to provide consistent results with experiments and empirical models [10] of flow through porous samples for a wide range of Reynolds numbers.

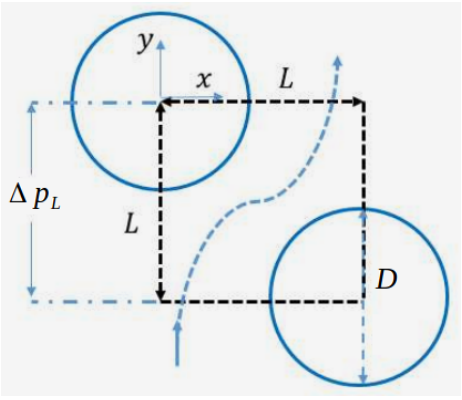

Figure 11: Sketch of staggered cylinders model (D is the diameter of each cylinder)

The characteristic length in the reference system of the pore cell sketched in figure 11 is L. The force that drives the flow through the pore cell is the pressure drop Δp_L between the two adjacent staggered cylinders. We can then define a characterist fluid-dynamic velocity U_c for this flow, which is linked to the pressure drop as

$$U_c = \sqrt{\frac{\Delta p_L}{\rho}} \,, \tag{25}$$

where ρ is the density of the flow in the pore cell. In the same way, we define the Reynolds number based on the characteristc velocity as

$$Re_c = \frac{\rho U_c L}{\mu} \,, \tag{26}$$

where μ is the flow viscosity in the pore cell. When assigning a porosity level (ϵ), the ratio D/L is automatically defined. Hence, the two main nondimensional parameters of the flow are Re_c and the ratio D/L (i.e. the porosity ϵ).

Let us consider now equation 19, which we rewrite for a single pore cell as follows,

$$\frac{\Delta p_L}{L} = \frac{\mu}{K} U + C\rho U^2 \,. \tag{27}$$

Note that U is not equal to U_c, as U_c represents a characteristic velocity, whereas U is the velocity solution of the fluid dynamic problem (as will be shown in the simulation results of Section 4.2.2). By introducing the Reynolds number based on the cylinder diameter,

$$Re_d = \frac{\rho U D}{\mu} \,, \tag{28}$$

and the Forchheimer coefficient, $F = CD$, equation 27 can be rearranged as,

$$\frac{\Delta p_L}{L} = \left(\frac{D^2}{K} + F Re_d \right) \frac{\mu U}{D^2} \,. \tag{29}$$

In the above equation, D^2/K represents the Darcy drag, and FRe_d represents the Forchheimer drag. By following Lee and Yang's [18] approach, the sum between the Darcy and the Forchheimer drag, i.e. the Darcy-Forchheimer drag ($D - F$), can be expressed as,

$$\left(\frac{D^2}{K} + F Re_d \right) = Re_c \left(\frac{D}{L} \right)^2 \frac{U_c}{U} = Re_c \left(\frac{D}{L} \right)^2 \frac{1}{q} \,, \tag{30}$$

in which the term q represents the average velocity along the cell outlet edge (or surface) normalised with the characteristic velocity ($q = U/U_c$), which can also be expressed in terms of the local velocity $v(x)$ at a generic location x along the surface as,

$$q = \frac{1}{U_C} \frac{1}{L} \int_0^L v dx \,. \tag{31}$$

A sketch of the velocity profile $v(x)$ on the pore surface can be seen in figure 12.

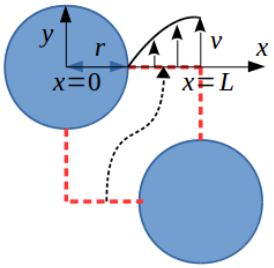

Figure 12: Sketch of the $v(x)$ velocity profile on the pore surface

By assigning the two main parameters of the simulation, namely the Reynolds number Re_c and the porosity ϵ, hence the geometrical factor D/L, simulations are conducted until a steady state is reached. The normalised velocity on the pore cell surface, q, represents the output of our numerical simulations, for each imposed Re_c at a fixed ϵ. Then, from each computed value of q, the corresponding value of Re_d can be computed through the relation

$$Re_d = Re_c \left(\frac{D}{L}\right) q \, . \tag{32}$$

The results of Lee and Yang [18] are reported in figure 13, for different porosity levels. Their numerical values of the $D-F$ drag were compared with the empirical results of Ergun [10] and the computational results of [17], for the same range of Reynolds numbers (Re_d) and porosities. As can be seen, a very good agreement with Ergun's empirical results was obtained at the porosity level $\epsilon = 0.43$, which is approximately equal to our considered porosity level (42 %).

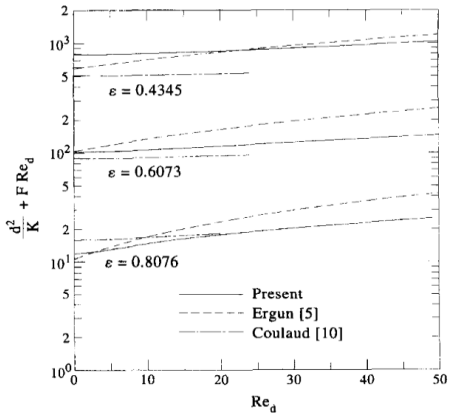

Figure 13: Result for the $D - F$ drag at different Re_d, from Lee and Yang [18]

The application of the above described procedure for our considered case will be the subject of the next sections.

4.2.2 Validation case

First, we have validated the computational model described in the previous section against the results of Lee and Yang [18], for different imposed Re_c. We adopt a configuration that is different to Lee and Yang's case, and more consistent with our considered experimental case [30]. In fact, instead of considering only a unit cell domain (as sketched in figure 11) and imposing a unit dimensionless presure drop ($\Delta p_L/p_\infty = 1$) across the cell, as in Lee and Yang's work, we consider a small flat-plate domain with periodic boundary conditions in the streamwise direction, five rows of cylinders in the y-direction, with imposed plenum conditions at the bottom boundary. A sketch of the configuration can be seen in figure 14.

We consider a configuration in the absence of a hypersonic crossflow, i.e. thinking that the plate model is at atmospheric conditions, but subject to the same pressure drop provided in the experiments of Hermann et al. [30]. Thus we consider atmospheric conditions outside of the porous layer in the initial state. Our dimensional reference values for pressure and density are then $\rho^*_\infty = 1.225$ kg/m^3, and $p^*_\infty = 1.013 \times 10^5$ Pa. We consider the normalised pressure drop measured in the experimental conditions, i.e. $\Delta p_{exp} = 148.5$ [30]. This corresponds to the pressure drop across the whole thickness of the porous sample ($\delta^* = 5$ mm). In order to compute the corresponding pressure drop for a unit pore cell (Δp_L), we assume the pressure descreases linearly from the plenum condition p_0 to the surface condition p_∞ (as sketched in figure 14), then we multiply the whole pressure drop by the ratio between the pore cell unit length L^* and the thickness δ^*, as

$$\Delta p_L = \Delta p_{exp} \frac{L^*}{\delta^*} \ . \tag{33}$$

The reference dimensional value considered for the pore cell length is $L^* = 9.9\,\mu$m, which corresponds to the value obtained by assuming a porosity of 42 % and a cylinder radius of $r^* = 6\,\mu$m (see Section 3). The minimum distance resulting from this pore size is $d^*_{min} = 2\,\mu$m, which is within the pore length scale range of the real porous sample. Hence, by the knowledge of L we can compute our reference Δp_L imposed in the simulations, which is $\Delta p_L = 0.29$. From our reference values in atmospheric conditions, p^*_∞ and ρ^*_∞, and from the corresponding dimensional value of the pressure drop, $\Delta p^* = 0.29 p^*_\infty$, we can now compute the characteristic velocity at the outlet of the porous layer, as $U^*_c = \sqrt{\Delta p^*/\rho^*_\infty} = 154.85$ m/s. A uniform temperature is imposed in the whole domain in the initial state, equal to the room temperature $T^*_\infty = 290$ K. From these values of the temperature and the characteristic velocity, the resulting Mach number of the simulation is $M = 0.45$. The pressure is normalised with the Mach number as described in Section 2.1, and within the porous layer the density follows the trend of the pressure through the equation of state, equation 13. All the velocity components are set to zero in the initial state.

Hence, summarising from the above described settings, the nondimensional parameters of our simulations are $M = 0.45$, the pressure drop $\Delta p = 0.29$, the ratio $D/L = 1.2$ (from 42 % porosity), and the Reynolds number Re_c, for which different values are imposed in different runs. Moreover, the usual Prandtl number of $Pr = 0.72$ and ratio of specific heats $\gamma = 1.4$ for air are considered.

It should be mentioned that, with these settings, the nondimensional value of L is 1 in our computational domain, as it is our reference length scale, and the velocity components are all normalised with the characteristic velocity U_c, which is fixed from the Mach number and the pressure drop, as described above. Thus, varying the Reynolds number Re_c, in our case, would correspond to varying the dimensional length scale L^* of the pore unit cell from a simulation to another.

The Reynolds number Re_c is varied from $Re_c = 5$ to $Re_c = 200$, to cover a relatively wide range of conditions. At each Re_c, the integral of the vertical velocity at the pore surface ($y = 0$) is evaluated, as sketched in figure 12, to obtain q from equation 31, and the corresponding granular Reynolds number Re_d is computed from equation 32. Finally, the Darcy-Forchheimer drag is evaluated from equation 30.

The computational domain sizes are $L_x = 4$ and $L_y = 14$, including an overall porous layer thickness of about 5.2. The grid size is $N_x \times N_y = 210 \times 700$, and simulations are conducted with one grid level.

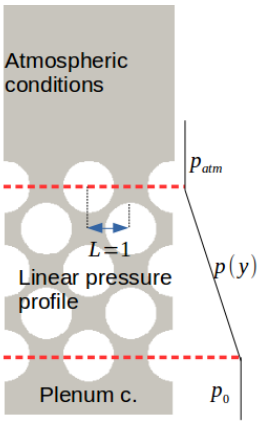

Figure 14: Sketch of the computational domain. In the initial state, atmospheric conditions are considered at the top (i.e. no crossflow)

The results of the validation study are shown in figure 15, where the trend of the computed $D - F$ drag is plotted against different values of the Reynolds number Re_d. As can be seen, our numerical results are in a very good agreement with the computational results of Lee and Yang [18] for a wide range of Reynolds numbers. A disagreement is observed only at very low Reynolds numbers ($Re_d < 1$), where our numerical results are observed to converge to results obtained from the empirical model of Ergun. This can be checked in figure 13, which is taken from the work of Lee and Yang [18], and that shows comparison with Ergun's empirical model at different values of the porosity. In our case, we consider a porosity of $\epsilon = 0.42$, thus very close to the value of 0.43 represented in the figure. The reason why our numerical model converges to the empirical model of Ergun at the very low Reynolds numbers, disagreeing with Lee and Yang's computational results, is that the latter do not solve the energy equation, in which the viscous dissipation terms play an important role at the very low Reynolds numbers.

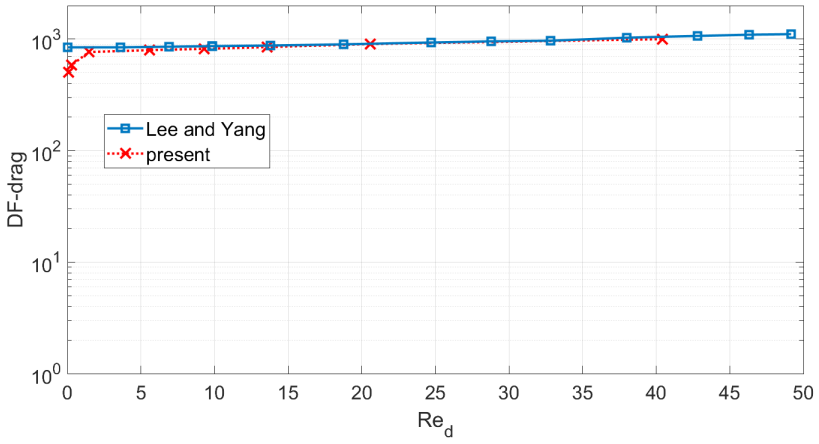

Figure 15: Result for the $D-F$ drag at different Re_d

Figure 16 shows results for the vertical velocity field inside and outside the porous layer in the domain considered in the simulations performed for the validation case. Only four rows of cylinders have been used across the porous layer, which demonstrates to be enough for providing the correct perssure drop solution, as seen in the validation results of figure 15. It should be mentioned that the pressure drop in relation 33 refers to a single porous cell. Hence, once a certain value of the pressure drop Δp_L is applied in combination with a certain L (i.e. a fixed porosity) for a single pore cell, the plenum pressure condition at the bottom boundary is applied by multiplying the single-cell pressure drop (Δp_L) by the total number of cells (or layers) generated by the rows of staggered cylinders (in this case four). Hence, the total pressure difference between the plenum chamber and the surface can be expressed as

$$\Delta p_{plenum} = p_0 - p_\infty = N \Delta p_L \ , \tag{34}$$

where $N = 4$ is the total number of pore cells in the vertical direction in this case ($N = n - 1$, with n indicating the total number of cylinder/sphere rows).

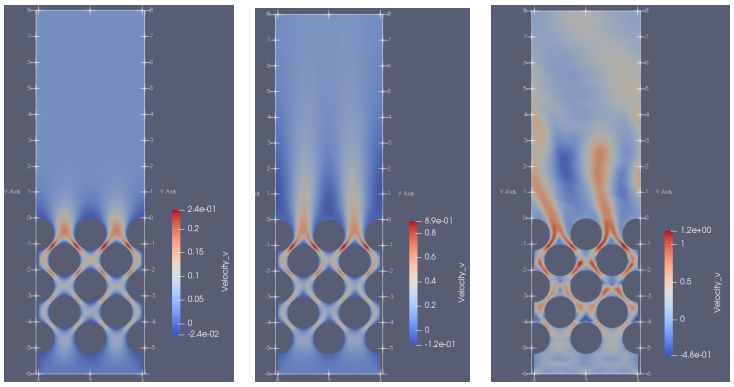

(a) $Re_c = 25$ (b) $Re_c = 100$ (c) $Re_c = 200$

Figure 16: Instantaneous vertical velocity field for the case without surface crossflow, at different Reynolds numbers

4.2.3 Equivalent D-F behaviour at different pore scales

After assessing the capabilities of the porous computational model, we want to develop and test a method for rescaling the pore size L to higher scales and obtaining at the same time an equivalent Darcy-Forchheimer drag. Each point on the $D - F$ curve in figure 15 corresponds to a certain Darcy-Forchheimer behaviour of the material, i.e. to a specific overall drag opposed by the porous layer to the traversing flow. Hence, the problem that we want to address is to increase the pore cell size of the porous structure while staying on a certain (generic) position (Re_d, $D - F$) on the $D - F$ graph. We refer to this strategy as a multiscale approach, whose relative description and validation is the subject of this section.

By looking at equations 30 and 32 we can observe that the main quantities on the ordinate and abscissa axes of figure 15, namely $D - F$ and Re_d, are both functions of the two parameters Re_c and D/L (i.e. ϵ), and of the resulting normalised velocity q (or U/U_c). We also notice that if we fix the porosity, ϵ, by varying the pore cell length scale L, the ratio D/L stays constant, as the diameter D will scale with L to provide the same porosity.

Now, in virtue of the fundamental principle of aerodynamics stating that two problems with a different scale magnitude can be considered similar, and hence share the same nondimensional flowfield solution, if they have the same shape and the same Reynolds number (as well as the other similarity parameters of the flow, namely M, Pr, γ), our considered problem reduces to keeping constant the characteristic Reynolds number Re_c. So, our assumption is that by imposing the same D/L (i.e. the shape of the porous structure) as well as the same Re_c, two problems with different pore size L will provide the same normalised solution q, which, in turn, will give the same values of $D-F$ and Re_d, i.e. the equivalent Darcy-Forchheimer behaviour. We want to prove this with application to the real hypersonic experimental case of Hermann et al. [30].

Let us consider the freestream conditions described in Section 3, which represent

the hypersonic flow conditions in Hermann et al.'s experiment [30]. We first need to calculate the characteristic Reynolds number (Re_c) representative of the flow through a single pore cell in these experimental conditions. The reference dimensional pore-cell size is, as mentioned in Section 4.2.2, $L^* = 9.9\,\mu$m, which provides a minimum length scale comparable with the porous microstructure of the real material sample, i.e. $d^*_{min} = 2\,\mu$m with $\epsilon = 0.42$. Following the procedure described in Section 4.2.2, we compute the dimensional characteristic velocity (U^*_c) by using the same normalised pressure drop, but, instead of using atmospheric conditions (as made in Section 4.2.2 for a case of no external crossflow), we consider now the experimental freestream conditions of the hypersonic crossflow [30]. The freestream conditions for density, pressure and temperature are $\rho^*_\infty = 0.074$ kg/m^3, $p^*_\infty = 1.632$ kPa, $T^*_\infty = 76.6$ K.

As already described in Section 4.2.2, we consider the experimental pressure drop measured by Hermann et al. [30], i.e.

$$\Delta p_{exp} = \left(\frac{\Delta p^*}{p^*_\infty} \right)_{exp} = 148.5 \,, \tag{35}$$

for the full sample thickness of $\delta^* = 5$ mm. From this value and from the reference pore-cell size L^*, we obtain the single-cell normalised pressure drop by equation 33, which gives $\Delta p_L = 0.29$. This value corresponds to a dimensional value of $\Delta p^*_L = p^*_\infty \Delta p_L = 0.473$ kPa.

In order to compute the characteristic velocity, it is helpful to refer to the sketch in figure 17. Contrarily to the case described in Section 4.2.2 of injection into atmospheric conditions with no crossflow, in this case we consider a single pore cell on the plate surface injecting fluid into a crossflow hypersonic boundary layer. Thus, the flow conditions of the coolant at the pore cell outlet are those relative to the isothermal wall conditions, which are denoted as T_w and ρ_w for temperature and density respectively. We recall that the wall temperature is fixed to the room temperature, i.e. $T^*_w = 290$ K, thus the normalised wall temperature is $T_w = 3.78$. This is also the temperature of the gas inside the plenum chamber ($T_{0,plenum} = T_w$). The pressure is assumed to be constant within the boundary layer, thus equal to the freestream conditions, i.e. $p_\infty = 1/\gamma M^2$ dimensionless. Due to the constant pressure within the boundary layer, the normalised density at the wall, from the equation of state 13, is $\rho_w = 1/T_w = 0.26$. In dimensional units, this density value corresponds to $\rho^*_w = 0.01924$ kg/m^3. Hence, the dimensional characteristic velocity is computed as

$$U^*_c = \sqrt{\frac{\Delta p^*_L}{\rho^*_w}} \,, \tag{36}$$

which gives a value of 156.79 m/s. The characteristic Reynolds number is then obtained as

$$Re_c = \frac{\rho^*_w U^*_c L^*}{\mu^*_w} = 1.67 \,, \tag{37}$$

where the dynamic viscosity μ^*_w was computed from the wall temperature by using Sutherland's law. This value of Re_c is small enough to allow the Forchheimer effects

to be neglected, and to consider the flow through the porous medium in the Darcy regime. This is indeed consistent with the very small length scales of the real material sample microstructure.

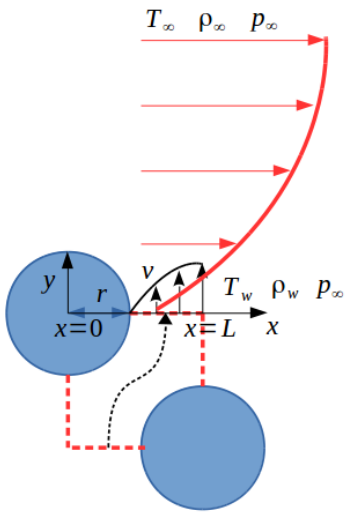

Figure 17: Sketch of a single pore cell on the surface injecting fluid into a crossflow boundary layer. The flow is at wall conditions at the injection location

Now that we have found a value of the characteristic Reynolds number representative of the inner pore length scales of the material sample, we need to find a relation that allows to keep the Reynolds number Re_c constant for increasing pore-cell length scales L. From the definitions 25 and 26 for the characteristic velocity and the characteristic Reynolds number, we can express Re_c in terms of the pore-cell pressure drop as

$$Re_c = \frac{\rho\sqrt{\frac{\Delta p_L}{\rho}}L}{\mu}\,, \tag{38}$$

from which, by rearranging, the pressure drop can be expressed as

$$\Delta p_L = \rho\left(\frac{Re_c\mu}{\rho L}\right)^2\,. \tag{39}$$

Now, we can use equation 39 to rescale the pressure drop with L by considering different pore sizes while keeping constant the Reynolds number Re_c and the porosity, i.e. the term D/L. We want to demonstrate that as long as we keep constant the parameters Re_c and D/L the solution of the Darcy-Forchheimer behaviour (i.e. $D-F$ and Re_d) can be considered similar, thus independent on the pore size.

We then perform simulations for four different cylinder diameters (at a fixed porosity of 42 %), namely $D^* = 12, 24, 48, 96$ μm. The smallest diameter ($D^* = 12\mu$m)

corresponds to the pore length scale of $L^* = 9.9\,\mu$m and the minimum length scale of 2 μm representative of the real porous sample inner scale in Hermann et al.'s experiment [30]. The ratio D/L is equal to 1.21 for all the cases.

Figure 18 shows the geometry used for the smallest diameter case, as well as a close-up of the qualitative solution obtained for the y-momentum within the porous layer. The configuration is similar to that decribed in Section 3, i.e. a small flat-plate domain with streamwise period boundary conditions, and a porous layer of a certain thickness and length placed in the middle of the domain. The boundary conditions are described in Section 3, with the plenum temperature set to 290 K, as the wall temperature. The characteristic length in the simulations is the initial boundary-layer displacement thickness of the similarity solution, i.e. 1 mm. For this case, the dimensionless domain sizes are $L_x = 1$ and $L_y = 3.4$. The dimensionless length of the porous layer is 0.5, and the thickness is 0.06. The radius of the circular particles is $r = 0.006$. Starting from the above-mentioned single pore cell pressure drop of $\Delta p_L = 0.29$, the overall pressure drop imposed through the whole porous layer is computed through equation 34 with a number of pore cells equal to $N = 6$. The base grid size is $N_x \times N_y = 400 \times 1360$, and three AMR levels have been used.

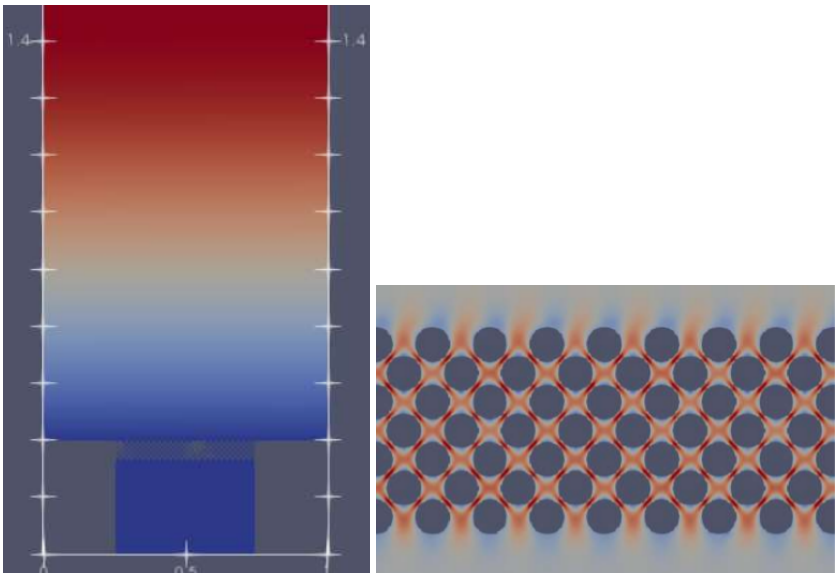

Figure 18: Streamwise velocity field (left) and close-up of y-momentum field in the porous layer (right), for the case $D^* = 12\mu$m

The computed blowing ratio ($F = \rho v|_{inj}$) profile along the outlet surface of a single pore cell is plotted in figure 19. The peak is reached in the middle of the jet, and is very close to the value of 2×10^{-3}, which is, in turn, the blowing ratio measured in the experiment of Hermann et al. [30]. Hence, this proves that the simulation with the smallest particle diameter (12 μm), providing a minimum inner length scale (2 μm) comparable with the real pore scale of the sample material, gives results in a good

agreement with the experimental case. A normalised velocity $q = 3.8 \times 10^{-3}$ was computed in this case, using equation 31 and the previously computed value of U_c^* using equation 36.

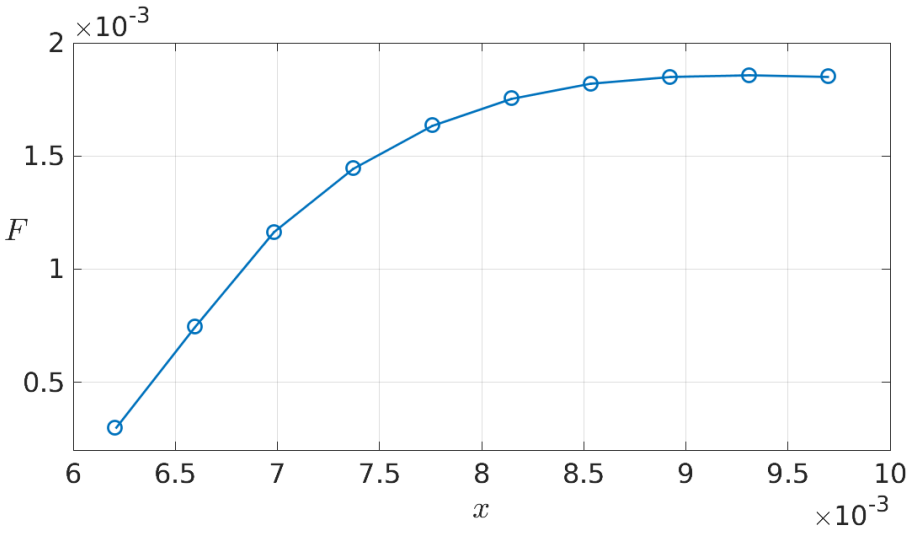

Figure 19: Blowing ratio profile along the outlet surface of a single pore cell

Now, we perform simulations for the larger cylinder diameters, and we compute the value of q for each case following the same procedure described above. In each case, a different pore-cell pressure drop (Δp_L) is considered, which scales with L^* through equation 39. Thus, an increasing pore cell size will provide a decreasing pressure drop, for a constant characteristc Reynolds number ($Re_c = 1.67$). As a result of a different pressure drop, also the characteristic velocity U_c^* will be different in each case, from equation 36. The flow conditions in the freestream and at the wall are the same in all the cases.

Figure 20 shows the domain and the streamwise velocity field for the higher pore size cases. The domain size and base grid size are the same in all the cases, and have been mentioned above for the smallest diameter case. The porous layer size is different in each case, instead. In particular, the porous layer covers the full domain length of 1 in all the higher diameter cases. The dimensionless thicknesses of the porous layer are 0.04, 0.08 and 0.16 for the cases $D^* = 24, 48, 96$ μm respectively. Moreover, contrarily to the lowest diameter case, for all the higher diameter cases $n = 3$ rows of cylinders have been used, corresponding to $N = 2$ pore cells across the layer. The corresponding AMR levels are 3, 2 and 1 for the cases $D^* = 24, 48, 96$ μm respectively.

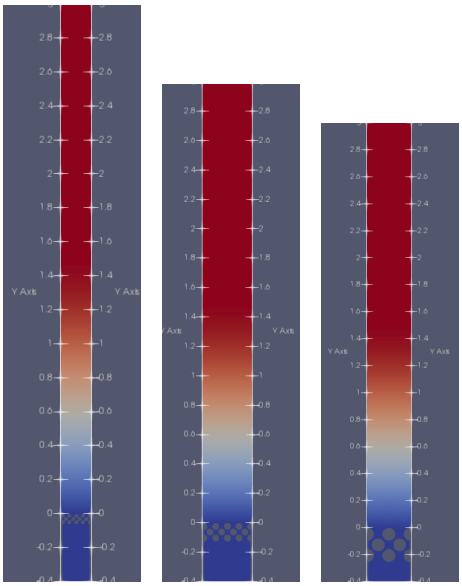

(a) $D^* = 24\,\mu$m (b) $D^* = 48\,\mu$m (c) $D^* = 96\,\mu$m

Figure 20: Periodic flat plate domains with underneath porous layer of different particle diameters. Streamwise velocity field plotted

The computed values of q for each case are listed in table 1. The good agreement between the computed values of q demonstrate that the considered problems at different pore sizes are similar, as they present the same solution, i.e. the equivalent $D-F$ drag, according to equation 30.

$D^* = 12\mu$m	$D^* = 24\mu$m	$D^* = 48\mu$m	$D^* = 96\mu$m
$q = 3.8 \times 10^{-3}$	$q = 3.7 \times 10^{-3}$	$q = 3.6 \times 10^{-3}$	$q = 3.8 \times 10^{-3}$

Table 1: Obtained numerical values for the velocity q

Finally, figure 21 shows details of the size effect on the injection flow features at the intake of each single pore for different pore sizes. The solution inside the porous layer is similar between the different cases, however a difference is observed in the amplitude of the spatial oscillations observed at the surface on the cylinder edges, representing localised shear layers of the vertical velocity, which are more pronounced for higher diameters of the cylinder.

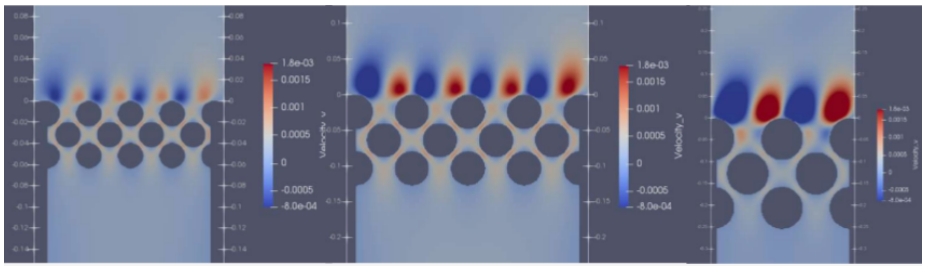

Figure 21: Vertical velocity field for the cases $D^* = 24\,\mu$m (left), $D^* = 48\,\mu$m (middle) and $D^* = 96\,\mu$m (right)

5 Conclusion

The present work has shown results from direct numerical simulations aimed at capturing the main physical features of flow injection through a porous layer over a flat plate in a hypersonic freestream, as well as the description and assessment of a methodology designed for the prediction of an equivalent Darcy-Forchheimer behaviour that mimics the real experimental material sample through a porous layer with higher inner pore length scales. The simulations have been based on experiments carried out in a hypersonic wind tunnel at Mach 5, with air injection through a sample of porous UHTC material, with a porosity of 42 %, and an inner pore length scale of the order of 1 to 4 μm.

A regular porous structure made of an arrangement of staggered cylinders with the same experimental porosity has been generated via an embedded boundary method to simulate the porous layer underneath of a flat plate, with plenum conditions imposed at the bottom boundary of the computational domain to simulate the presence of a plenum chamber.

Two-dimensional simulations have been performed for a porous layer made of circular particles with a diameter of 12 μm, which provides a minimum inner length scale of 2 μm, consistent with the real sample microstructure. The results have been shown to be in a good agreement with the experiments in terms of the blowing ratio on the surface. Then, a methodology based on former computational studies has been considered and further extended with the intent of demonstrating the similarity between cases with different pore size and constant characteristic Reynolds number Re_c of the flow through a single pore cell.

Results of simulations carried out for higher cylinder diameters, namely 24 μm, 48 μm and 96 μm, have shown that, by keeping constant the characteristic Reynolds number Re_c and the porosity ϵ, and by opportunely rescaling the pressure drop with the imposed pore size L through a formula derived from the definitions of characteristic Reynolds number and characteristic velocity U_c, two problems with different pore size share the same solution in terms of the developed Darcy-Forchheimer drag. Thus, this demonstrates that a computational model of the porous layer with a higher pore size providing an equivalent Darcy-Forchheimer behaviour to the smaller reference experimental microstructure scale can be obtained, which in turn allows the complex flow

features of injection in a hypersonic crossflow over a porous surface to be accurately resolved by means of computationally affordable direct numerical simulations.

The present findings are considered to be potentially of great importance for future studies aimed at the correct design and optimisation of new-generation transpiration cooling systems for hypersonic flight.

Acknowledgments

The authors would like to acknowledge support from EPSRC (Engineering and Physical Sciences Research Council) under the Grant No. EP/P000878/1.

References

[1] A. Fitt, J. Ockendon, T. Jones, Aerodynamics of slot-film cooling: theory and experiment, Journal of fluid mechanics 160 (1985) 15–27.

[2] A. Fitt, P. Wilmott, Slot film coolingthe effect of separation angle, Acta mechanica 103 (1-4) (1994) 79–88.

[3] S. Wittig, A. Schulz, M. Gritsch, K. A. Thole, Transonic film-cooling investigations: effects of hole shapes and orientations, in: ASME 1996 International Gas Turbine and Aeroengine Congress and Exhibition, American Society of Mechanical Engineers, 1996, pp. V004T09A026–V004T09A026.

[4] S. Baldauf, A. Schulz, S. Wittig, High-resolution measurements of local heat transfer coefficients from discrete hole film cooling, Transactions of the ASME-T-Journal of Turbomachinery 123 (4) (2001) 749–757.

[5] J. Meinert, J-ograve, r. Huhn, E. Serbest, O. J. Haidn, Turbulent boundary layers with foreign gas transpiration, Journal of Spacecraft and Rockets 38 (2) (2001) 191–198.

[6] T. Langener, J. V. Wolfersdorf, J. Steelant, Experimental investigations on transpiration cooling for scramjet applications using different coolants, AIAA journal 49 (7) (2011) 1409–1419.

[7] K. Heufer, H. Olivier, Experimental and numerical study of cooling gas injection in laminar supersonic flow, AIAA journal 46 (11) (2008) 2741–2751.

[8] M. A. Keller, M. J. Kloker, H. Olivier, Influence of cooling-gas properties on film-cooling effectiveness in supersonic flow, Journal of Spacecraft and Rockets 52 (5) (2015) 1443–1455.

[9] M. A. Keller, M. J. Kloker, Direct numerical simulation of foreign-gas film cooling in supersonic boundary-layer flow, Aiaa Journal 55 (1) (2016) 99–111.

[10] S. Ergun, A. A. Orning, Fluid flow through randomly packed columns and fluidized beds, Industrial & Engineering Chemistry 41 (6) (1949) 1179–1184.

[11] I. Macdonald, M. El-Sayed, K. Mow, F. Dullien, Flow through porous media-the ergun equation revisited, Industrial & Engineering Chemistry Fundamentals 18 (3) (1979) 199–208.

[12] E. Erdim, Ö. Akgiray, İ. Demir, A revisit of pressure drop-flow rate correlations for packed beds of spheres, Powder technology 283 (2015) 488–504.

[13] J. Kozeny, Uber kapillare leitung der wasser in boden, Royal Academy of Science, Vienna, Proc. Class I 136 (1927) 271–306.

[14] A. W. Heijs, C. P. Lowe, Numerical evaluation of the permeability and the kozeny constant for two types of porous media, Physical Review E 51 (5) (1995) 4346.

[15] P. C. Carman, Fluid flow through granular beds, Chemical Engineering Research and Design 75 (1997) S32–S48.

[16] M. Matyka, A. Khalili, Z. Koza, Tortuosity-porosity relation in porous media flow, Physical Review E 78 (2) (2008) 026306.

[17] O. Coulaud, P. Morel, J. Caltagirone, Numerical modelling of nonlinear effects in laminar flow through a porous medium, Journal of Fluid Mechanics 190 (1988) 393–407.

[18] S. Lee, J. Yang, Modeling of darcy-forchheimer drag for fluid flow across a bank of circular cylinders, International journal of heat and mass transfer 40 (13) (1997) 3149–3155.

[19] N. Jeong, D. H. Choi, C.-L. Lin, Prediction of darcy–forchheimer drag for microporous structures of complex geometry using the lattice boltzmann method, Journal of Micromechanics and Microengineering 16 (10) (2006) 2240.

[20] J. D. Anderson, Hypersonic and High-Temperature Gas Dynamics, Second Edition, AIAA Education Series, 2006.

[21] P. D. Neufeld, A. Janzen, R. Aziz, Empirical equations to calculate 16 of the transport collision integrals ω (l, s)* for the lennard-jones (12–6) potential, The Journal of Chemical Physics 57 (3) (1972) 1100–1102.

[22] D. J. Hill, D. I. Pullin, Hybrid tuned center-difference-weno method for large eddy simulations in the presence of strong shocks, Journal of Computational Physics 194 (2) (2004) 435–450.

[23] C. Pantano, R. Deiterding, D. J. Hill, D. I. Pullin, A low numerical dissipation patch-based adaptive mesh refinement method for large-eddy simulation of compressible flows, Journal of Computational Physics 221 (1) (2007) 63–87.

[24] J. L. Ziegler, R. Deiterding, J. E. Shepherd, D. I. Pullin, An adaptive high-order hybrid scheme for compressive, viscous flows with detailed chemistry, Journal of Computational Physics 230 (20) (2011) 7598–7630.

[25] M. Ihme, Y. Sun, R. Deiterding, Detailed simulations of weak-to-strong ignition of a h 2/o 2/ar mixture in shock-tubes, in: International Symposium on Shock Waves, Springer, 2013, pp. 209–214.

[26] A. Cerminara, R. Deiterding, N. Sandham, Dns of hypersonic flow over porous surfaces with a hybrid method, in: 2018 AIAA Aerospace Sciences Meeting, 2018, p. 0600.

[27] A. Cerminara, R. Deiterding, N. Sandham, Dns of hypersonic flow over porous surfaces with a hybrid method, in: 2018 AIAA Aerospace Sciences Meeting, 2018, p. 0600.

[28] R. Deiterding, Construction and application of an amr algorithm for distributed memory computers, in: Adaptive Mesh Refinement-Theory and Applications, Springer, 2005, pp. 361–372.

[29] R. Deiterding, Block-structured adaptive mesh refinement-theory, implementation and application, in: Esaim: Proceedings, Vol. 34, EDP Sciences, 2011, pp. 97–150.

[30] T. Hermann, H. S. Ifti, M. McGilvray, L. Doherty, R. P. Geraets, Mixing characteristics in a hypersonic flow around a transpiration cooled flat plate model, in: HiSST: International Conference on High-Speed Vehicle Science Technology, Moscow, Russia, 2018.

[31] R. Deiterding, Block-structured adaptive mesh refinement-theory, implementation and application, in: Esaim: Proceedings, Vol. 34, EDP Sciences, 2011, pp. 97–150.